Chemical Science

ROYAL SOCIETY OF CHEMISTRY

EDGE ARTICLE

View Article Online
View Journal | View Issue

Cite this: *Chem. Sci.*, 2022, **13**, 7172

All publication charges for this article have been paid for by the Royal Society of Chemistry

Tailoring a robust Al-MOF for trapping C_2H_6 and C_2H_2 towards efficient C_2H_4 purification from quaternary mixtures†

Subhajit Laha, Nimish Dwarkanath, Abhishek Sharma, Darsi Rambabu, Sundaram Balasubramanian * and Tapas Kumar Maji *

Received 25th February 2022
Accepted 15th May 2022

DOI: 10.1039/d2sc01180h

rsc.li/chemical-science

Light hydrocarbon separation is considered one of the most industrially challenging and desired chemical separation processes and is highly essential in polymer and chemical industries. Among them, separating ethylene (C_2H_4) from C2 hydrocarbon mixtures such as ethane (C_2H_6), acetylene (C_2H_2), and other natural gas elements (CO_2, CH_4) is of paramount importance and poses significant difficulty. We demonstrate such separations using an Al-MOF synthesised earlier as a non-porous material, but herein endowed with hierarchical porosity created under microwave conditions in an equimolar water/ethanol solution. The material possessing a large surface area (793 $m^2\ g^{-1}$) exhibits an excellent uptake capacity for major industrial hydrocarbons in the order of C_2H_2 > C_2H_6 > CO_2 > C_2H_4 > CH_4 under ambient conditions. It shows an outstanding dynamic breakthrough separation of ethylene (C_2H_4) not only for a binary mixture (C_2H_6/C_2H_4) but also for a quaternary combination ($C_2H_4/C_2H_6/C_2H_2/CO_2$ and $C_2H_4/C_2H_6/C_2H_2/CH_4$) of varying concentrations. The detailed separation/purification mechanism was unveiled by gas adsorption isotherms, mixed-gas adsorption calculations, selectivity estimations, advanced computer simulations such as density functional theory (DFT), grand canonical Monte Carlo (GCMC) and *ab initio* molecular dynamics (AIMD), and stepwise multicomponent dynamic breakthrough experiments.

Introduction

Purification and separation of chemical mixtures account for about 15% of total industrial energy consumption and are expected to increase nearly three times in the next twenty years as demand increases sharply in chemical industries.[1,2] At present, industry performs separation by utilising two major classical techniques, either *via* cryogenic distillation or a solvent extraction process.[3] However, these separation technologies are impaired by high energy penalties, while adsorptive separation using porous materials is environmentally friendly, effortless, and energetically inexpensive, which would save 80% of total energy expenditure.[4] The separation of several bulk chemical commodities involving light hydrocarbons (ethane, C_2H_6; ethylene, C_2H_4; acetylene, C_2H_2; methane, CH_4; *etc.*), which are the kernels of much industrial manufacturing, poses significant challenges due to their comparable shapes, volatilities and other physicochemical properties.[5,6]

C_2H_4 is the most commercially significant as it has exceeded an annual global production of 200 million tonnes.[7,8] Conventionally, C_2H_4 is obtained through steam cracking, catalytic/oxidative dehydrogenation and thermal decomposition of naphtha or C_2H_6, in which a certain amount of C_2H_6 and C_2H_2 co-exists and needs to be removed to produce polymer grade C_2H_4, broadly utilised in polymer, fibre and chemical industries.[9–11] In this process, C_2H_2 is primarily expelled through catalytic hydrogenation by using noble metal catalysts with the requirement of high pressure and temperature.[12,13] This C_2H_2 can act as a spoiler by reacting with catalytic metals to form acetylides, which have been known to engender explosion by blocking the gas flow. Within the same process, C_2H_6 is later separated from C_2H_4 by an energy-intensive high-pressure cryogenic distillation, typically at 5–28 bar and 183–258 K, which accounts for a notable hike in C_2H_4 price.[14–16] The separation of C_2H_6/C_2H_4 is presently considered the most challenging industrial separation, owing to similar molecular shapes (C_2H_4: 3.28 × 4.18 × 4.84 $Å^3$; C_2H_6: 3.81 × 4.08 × 4.82 $Å^3$) and boiling points (169.42 K for C_2H_4 and 184.55 for C_2H_6).[6,17,18] Concomitantly, the simultaneous removal of C_2H_6 and C_2H_2 through a more energy-efficient route with a single-step and reduced energy footprint for C_2H_4 production would be of industrial relevance.

Chemistry and Physics of Materials Unit, School of Advanced Materials (SAMat), Jawaharlal Nehru Centre for Advanced Scientific Research, Jakkur Post, Bangalore, 560064, India. E-mail: tmaji@jncasr.ac.in; bala@jncasr.ac.in; Web: https://www.jncasr.ac.in/tmaji

† Electronic supplementary information (ESI) available. See https://doi.org/10.1039/d2sc01180h

At the same time, C_2H_2 is also considered a major feedstock for polymer, polyester, plastic and chemical industries in the synthesis of essential organic compounds, including acrylic acid derivatives, α-ethynyl alcohols and vinyl compounds.[19,20] C_2H_2 is mainly produced by thermal cracking or partial combustion of hydrocarbons including naphtha or natural gas, co-existing with spin-offs such as C_2H_4, CO_2 and CH_4.[19,21,22] Purification of C_2H_2 from CO_2 is enormously challenging due to similarities in shape (C_2H_2: 3.32 × 3.34 × 5.7 Å^3; CO_2: 3.18 × 3.33 × 5.36 Å^3), boiling point (189.3 K for C_2H_2 and 194.7 K for CO_2) and other physical properties (polarizabilities of C_2H_2 and CO_2 are 19.5 and 33.3–39.3, respectively).[23] As an alternative, being acquired as a by-product in petroleum refining, C_2H_4 is also refined on an industrial scale from natural gas (CH_4 ∼ 70–90%, CO_2 ∼ 0–10%, C_2H_6 and C_2H_4 ∼ 1–15%).[24] As an outcome of similar physicochemical properties, it is most desirable but extremely complex to purify C_2H_4 from its associated bi-components, in particular C_2H_6, C_2H_2, CO_2 and CH_4 (Table S1†), through a one-step purification technique.

In the last two decades, great efforts have been undertaken in designing metal–organic frameworks (MOFs) as promising sorbents for various gas separations ranging from the simple N_2/CO_2 or H_2/CO_2 to the most challenging one such as olefin/paraffin by modulating the surface area, pore geometry, supramolecular and adsorbate–adsorbent interactions dictated by thermodynamic and kinetic preferences. To avail the preferential selectivity in MOFs, a few strategies have been generally adopted: (i) tuning the pore size/shapes, (ii) introducing functional organic linkers to generate strong binding sites, (iii) decorating the pore environment for favoured polarity and (iv) enhancing the density of open-metal sites (OMSs) for stronger interaction with unsaturated hydrocarbons.[25–29] MOFs with open-metal sites customarily adsorb C_2H_4 over C_2H_6 as a consequence of electrostatic interaction between the π–electrons of C_2H_4 and the positively charged metal centres.[30–33] However, this process leads to the preferential adsorption of C_2H_4, and releases C_2H_6 first, while C_2H_4 has to be recovered through heating or purging with an inert gas. Alternatively, this problem can be solved by employing C_2H_6 selective MOFs, which not only improves the purity of the liberated C_2H_4 but also avoids the multistep separation process by reducing energy expenditure.[5] To date, only a few hydrophobic or less polar MOFs have been reported with low separation performance as the hydrophobic space is hardly capable of distinguishing non-polar C_2H_6 and C_2H_4.[15,34–39] Yet, MOFs exhibiting such reverse adsorption phenomena of preferential C_2H_6 and C_2H_2 selectivity over C_2H_4 are still rare as of now.[40–42]

The Al-NDC ($[Al(OH)(1,4\text{-NDC})]\cdot 2H_2O$) MOF has high thermal and chemical stability with a robust 3D structure containing naphthalene moieties through the channel walls with distinct pore channels with sizes 3 × 3 Å^2 (small pore channel) and 7.7 × 7.7 Å^2 (large pore channel), respectively (Scheme 1).[43] Here, we report the exclusive, unrivalled performance of an Al-MOF, an adsorbent displaying strong preferential adsorption of C_2H_2 and C_2H_6 over C_2H_4. The microwave heating enables faster nucleation that helps the formation of smaller particle sizes with an increased surface-to-volume ratio.[44] Additionally, the mixed solvent duo, water–ethanol clusters act as templates for additional mesopore formation and corresponding hierarchical porosity in the framework.[45] This investigation unfolds the impact of reaction time, ranging from 5 to 220 minutes, wherein the MOF produced with 15 minutes (Al-MOFM$_{15}$) of

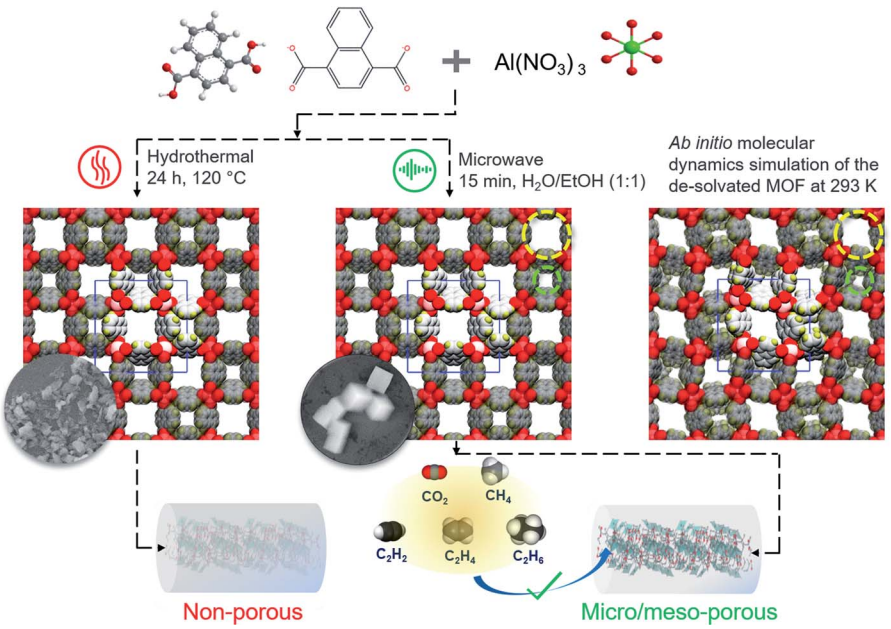

Scheme 1 Schematic representation of the hydrothermal (left) and microwave heating (right) synthesis strategy for Al-MOF and Al-MOFM$_{15}$, respectively. The corresponding insets are the FESEM images showing the morphologies of Al-MOF and Al-MOF$_{15}$, respectively (see Fig. S2†). A small and a large pore channel are identified in green and yellow dashed circles, respectively. *Ab initio* molecular dynamics simulation of the de-solvated MOF at 293 K shows spontaneous closure of the small pore channels (extreme right).

reaction time showed the maximum surface area (BET; 793 $m^2 g^{-1}$) with the highest micro–mesopore volume ratio. Al-MOFM$_{15}$ turned out to be an efficient adsorbent for the purification of C_2H_4 from the binary C_2H_6/C_2H_4 and quaternary $C_2H_4/C_2H_6/C_2H_2/CO_2$ and $C_2H_4/C_2H_6/C_2H_2/CH_4$ mixtures based on dynamic breakthrough studies. The C_2H_2/CO_2, C_2H_6/CH_4 and CO_2/CH_4 separation performances were also examined under ambient conditions. The key separations were performed through a stepwise dynamic breakthrough technique to obtain each component with high purity; the MOF retained its performance over multiple cycles, without any temperature swing desorption, and promises to be an efficient, major C2 hydrocarbon sorting tool in future industrial separation processes.

Results and discussion

Synthesis and characterisation

The non-porous Al-NDC ($[Al(OH)(1,4\text{-NDC})]\cdot 2H_2O$) MOF was selected and synthesised by the hydrothermal reaction of 1,4-naphthalenedicarboxylate and $Al(NO_3)_3\cdot 9H_2O$, according to the previously reported method.[43] Al-NDC MOF was also synthesised under microwave heating conditions by tailoring the reaction times (5, 15, 30, 60, 120 and 220 minutes) with the assistance of the water/ethanol (1 : 1) solvent duo and six different products, namely Al-MOFM$_5$, Al-MOFM$_{15}$, Al-MOFM$_{30}$, Al-MOFM$_{60}$, Al-MOFM$_{120}$, and Al-MOFM$_{220}$, respectively ('M' stands for microwave and the subscript represents the reaction time in minutes) were isolated (see the ESI†).[45] The similarity in powder X-ray diffraction (PXRD) patterns with that of the simulated pattern revealed the formation of a similar three-dimensional framework with two square-shaped cross-sectional channels (Fig. S1†). As reported by us previously, the microwave heating enables faster nucleation that improves the structural porosity by enhancing the surface-to-volume ratio based on particle downsizing.[44–46] N_2 adsorption experiments were performed at 77 K (Fig. S3†) to establish permanent porosity and Al-MOFM$_5$, Al-MOFM$_{15}$, Al-MOFM$_{30}$, Al-MOFM$_{60}$, Al-MOFM$_{120}$, Al-MOFM$_{220}$ with BET surface areas estimated to be 759, 793, 731, 694, 682 and 664 $m^2 g^{-1}$, respectively (Fig. S4†). The N_2 adsorption isotherms for Al-MOFM$_5$ and Al-MOF$_{15}$ exhibited a characteristic type-I profile corresponding to a microporous nature, whereas Al-MOFM$_{30,60,120,220}$ showed additional mesopore formation with the combination of type-I and type-IV isotherms (Fig. S3a†). The NLDFT (non-local density functional theory) model-based pore-size distribution analysis reveals the presence of mesopores with a size of about 3.6 nm with a gradual decrease in surface area and the corresponding micro-to-mesopore volume ratios for post-30 min reaction times (Fig. S3b and S4†). There are a few reports of low polarity or hydrophobic MOFs[39,47,48] with high surface areas including structural rigidity, desirable pore aperture, and fascinating thermal and chemical stabilities with excellent moisture robustness.[49–52] Thus, the remarkable surface area with

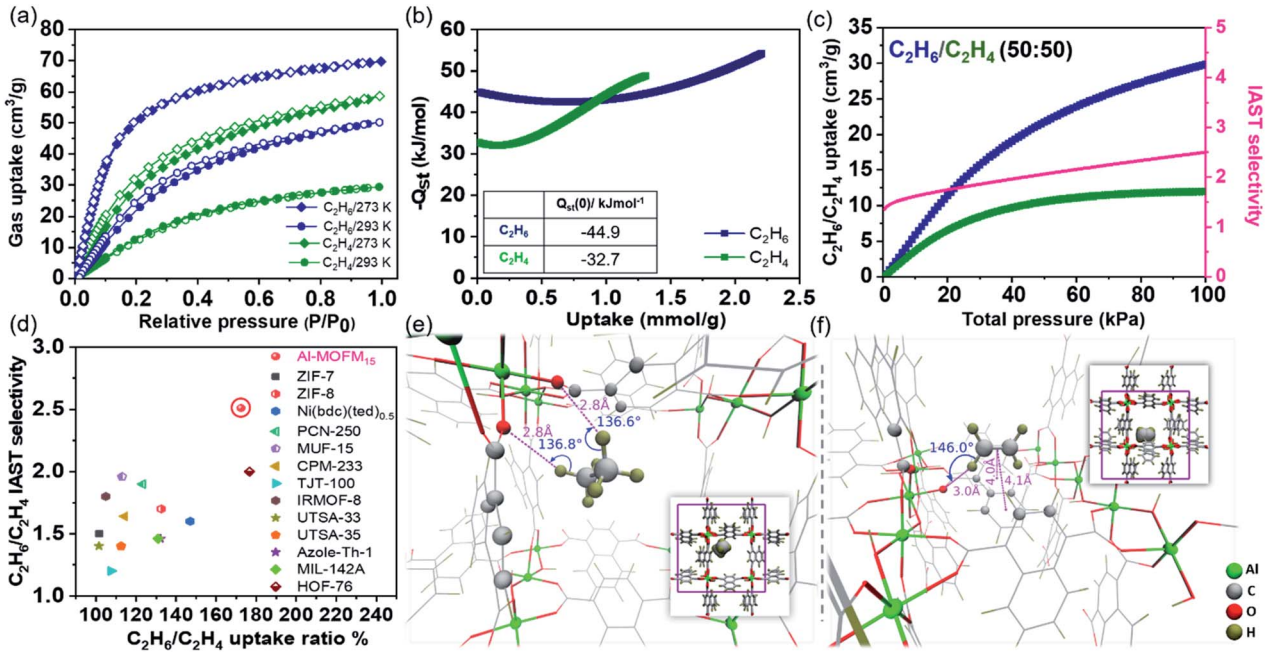

Fig. 1 (a) Single-component adsorption–desorption isotherms of C_2H_6 and C_2H_4 in Al-MOFM$_{15}$ measured at 273 and 293 K for pressures 0–690 torr. (b) Isosteric heats of adsorption (Q_{st}) of C_2H_6 and C_2H_4 at various loading amounts (near-zero coverage Q_{st} values are provided in the inset). (c) Mixed adsorption isotherms and selectivity calculated using IAST for C_2H_6/C_2H_4 (50 : 50) in Al-MOFM$_{15}$ at 293 K. (d) C_2H_6/C_2H_4 separation performance in some benchmark porous materials. (e and f) Locations of the highest binding affinity sites determined by DFT optimization for C_2H_6 (−39.9 kJ mol^{-1}) and C_2H_4 (−38.7 kJ mol^{-1}). Insets: Corresponding molecule locations, zoomed out, within the large channel. C_2H_6 participates in two hydrogen-bonding interactions with carboxylate oxygens while C_2H_4 participates in π–π and hydrogen-bonding interactions with the naphthalene ring and carboxylate oxygen, respectively. Binding sites with lower affinities for C_2H_4 and C_2H_6 are shown in Fig. S23 and S24,† respectively.

exclusive microporosity (centred at 1.2 nm) of Al-MOFM$_{15}$ prompted us to investigate its light hydrocarbon adsorption and separation properties.

Single-component hydrocarbon adsorption and mixed-gas selectivity calculation

Single component adsorption–desorption isotherms for CO_2, CH_4, C_2H_2, C_2H_4, and C_2H_6 were studied using activated Al-MOFM$_{15}$ at 293 and 273 K. As shown in Fig. 1a and 2a, the saturation uptake amounts for C_2H_2, C_2H_6, CO_2, C_2H_4, and CH_4 are 64 (2.85 mmol g^{-1}), 50 (2.23 mmol g^{-1}), 40 (1.785 mmol g^{-1}), 29 (1.29 mmol g^{-1}) and 14 (0.625 mmol g^{-1}) mL g^{-1} (or cm^3 g^{-1}) at 293 K, respectively. The isosteric heats of adsorption (Q_{st}) were estimated with the Clausius–Clapeyron equation by fitting the isotherms using the virial expression and Freundlich–Langmuir (FL) isotherm models at 273, 283 and 293 K (Fig. S6–S12†).[53] Q_{st} estimated by virial and FL-fitting are in qualitative agreement for the five gases; we use the ones obtained using virial fitting for the discussion that follows. The order of resultant Q_{st} at near-zero coverage ($Q_{st}(0)$) is C_2H_6 (−45.0 kJ mol^{-1}) > C_2H_2 (−40.2 kJ mol^{-1}) > C_2H_4 (−32.8 kJ mol^{-1}) > CO_2 (−24.6 kJ mol^{-1}) > CH_4 (−22.0 kJ mol^{-1}). Notably, the adsorption enthalpies for CO_2 and C_2H_2 do not vary substantially with loading suggesting uniformity in binding sites (Fig. 2b). On the other hand, high polarizability endorses a relatively greater affinity for C_2H_6 among C2 hydrocarbons (Table S4†). For C_2H_4, as shown in Fig. 1b, the adsorption enthalpy rapidly increases with the loading amount because of probable π···π and C–H···π interactions among guests. Most importantly, under dilute conditions, C_2H_6 has higher binding affinity compared to that of C_2H_4 by about 12 kJ mol^{-1}, greater than in any other benchmark porous materials reported so far (Fig. S13 and Table S6†). As documented in Table S1,† C_2H_6–C_2H_4 separation is extremely challenging because of comparable physical properties. C_2H_4 (1.5×10^{-26} esu cm^2) has a higher quadrupole moment over C_2H_6 (0.65×10^{-26} esu cm^2), making the process of fabricating C_2H_4-selective MOFs relatively straightforward, for example, by incorporating unsaturated metal sites or a hydrogen-bonding acceptor to stimulate the selectivity.[31,54] Achieving the reverse, *i.e.*, enabling the preferential sorption of C_2H_6 over C_2H_4 is non-trivial, which can simplify the separation process by selectively releasing pure C_2H_4 from the downstream outlet.[5,55] On a similar note, separating C_2H_2/CO_2 is equally complex as a consequence of cognate molecular dimensions (C_2H_2: 3.32 × 3.34 × 5.7 Å^3 and CO_2: 3.18 × 3.33 × 5.36 Å^3) and boiling points (C_2H_2, 189.3 K; CO_2, 194.7 K). The higher uptake ratio of C_2H_6 over C_2H_4 and C_2H_2 over CO_2 in Al-MOFM$_{15}$ motivated us to study the nature of hydrocarbon binding interaction in its pore channels. In addition, the adsorption kinetics of CO_2 and CH_4 are analysed by fitting it into the LDF (linear driving force) model at the first adsorption point ($P \sim 4$ kPa). CO_2 shows a faster rate of adsorption with a rate constant value of 0.184 compared to CH_4 ($k = 2.25 \times 10^{-3}$; Fig. S14†).

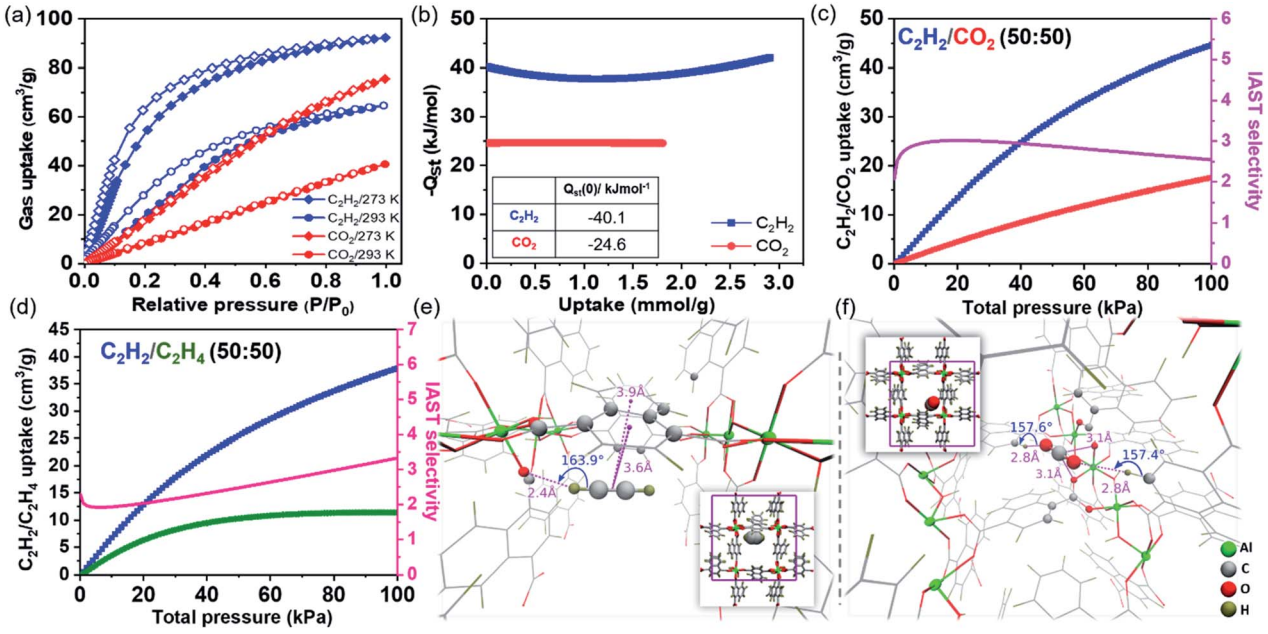

Fig. 2 (a) Single-component adsorption–desorption isotherms of C_2H_2 and CO_2 in Al-MOFM$_{15}$ measured at 273 and 293 K for pressures 0–690 torr. (b) Isosteric heats of adsorption (Q_{st}) of C_2H_2 and CO_2 at various loading amounts (Q_{st} values at near-zero coverage area are provided in the inset). (c and d) Mixed adsorption isotherms and selectivity calculated using IAST for (c) C_2H_2/CO_2 (50 : 50) and (d) C_2H_2/C_2H_4 (50 : 50) in Al-MOFM$_{15}$ at 293 K. (e and f) Locations of the highest binding affinity sites determined by DFT optimization for C_2H_2 (−37.3 kJ mol^{-1}) and CO_2 (−36.0 kJ mol^{-1}), respectively. Insets show the positions of the guest molecules within the square cross-section of a large pore, while the corresponding main panels show their neighbourhood. C_2H_2 participates in π–π and hydrogen-bonding interactions with a naphthalene ring and a carboxylate oxygen, respectively, while CO_2 interacts with two naphthalene hydrogens and a carboxylate oxygen *via* hydrogen-bonding and Lewis acid–base interactions, respectively. Binding sites with lower affinities for CO_2 and C_2H_2 are shown in Fig. S21 and S22,† respectively.

Next, to estimate the adsorption isotherm and adsorption selectivity for the equimolar composition of gases under ambient (293 K, 1 bar) and near ambient conditions (273 K, 1 bar; Fig. S17–S20†), ideal adsorption solution theory (IAST)[56] was employed. The Freundlich–Langmuir model was used to fit single-component experimental adsorption isotherms (at 273 and 293 K). The calculated bi-component equimolar C_2H_6/C_2H_4 adsorption isotherms are shown in Fig. 1c. The mixed adsorption amounts at 100 kPa for C_2H_6 and C_2H_4 are 41 and 29 mL g^{-1}, respectively, whereas, for the C_2H_2/CO_2 combination, the individual saturation uptakes are 44 and 17 mL g^{-1} (Fig. 1c, 2c and Table S3†). The selectivity value rises with increasing gas pressure for C_2H_6/C_2H_4, confirming the real separation ability of Al-MOFM$_{15}$ under practical conditions. The selectivity of C_2H_6 over C_2H_4 exceeds most reported top-performing porous materials (Fig. 1d; Tables S3 and S6†). For C_2H_2/CO_2, the selectivity factor reaches a maximum (3.018) at 20 kPa, and further drops with an increase in pressure (Fig. 2c).[57,58] In contrast, C_2H_2/C_2H_4 selectivity drops to a minimum before exhibiting a monotonically increasing behaviour (Fig. 2d).[59] As shown in Fig. 1c, 2c and d, the adsorption selectivities for C_2H_6/C_2H_4, C_2H_2/CO_2 and C_2H_2/C_2H_4 at a pressure of 100 kPa were calculated to be 2.51, 2.54 and 3.32, respectively. For other equimolar mixtures, the selectivities of C_2H_2/C_2H_4, C_2H_6/CH_4, CO_2/CH_4 and C_2H_2/CH_4 are 6.15, 2.9, 3.32 and 7.12, respectively at 100 kPa at ambient temperature (293 K). To the best of our knowledge, Al-MOFM$_{15}$ is one of those rare porous materials that show such a high selectivity in the range of 2 to 8 for all light hydrocarbon mixtures under ambient conditions (100 kPa and 293 K; Tables S3, S6 and S7†).[60,61] In addition, Grand Canonical Monte Carlo (GCMC) simulations were also performed to theoretically calculate single-component adsorption isotherms. As shown in Fig S41,† the isotherms were obtained by performing the simulations after blocking the small pore channels of Al-MOF. Although these isotherms showed lower uptake than those obtained by not imposing any such restriction on where the molecules were adsorbed, they continued to overpredict the uptake amounts compared to the experimental observations; disregarding the flexibility of the naphthalene rings in the GCMC simulations could be a plausible reason for the overprediction.

Insights from molecular simulations

To understand the interactions governing single component adsorption, a combination of advanced molecular simulation tools was employed to (a) gain better insights into the binding sites and adsorption affinities of a diverse set of guest molecules—CO_2, C_2H_2, C_2H_4, C_2H_6, and CH_4 inside Al-MOF and (b) elucidate the underlying microscopic reasons for the crossover in Q_{st} *vs.* uptake between C_2H_4 and C_2H_6 (Fig. 1b). We set out to identify binding sites only in the large pore channels (Fig. S16†) because of the following factors: (i) ^{129}Xe NMR studies by Comotti *et al.*[43] showed that xenon adsorption into the small pore channels (3×3 Å^2) was negligible. However, the smallest dimension of any of the guests considered in the present work is well over 3 Å. (ii) To gain additional insights, a five pico-second *ab initio* molecular dynamics (AIMD) trajectory of the desolvated MOF at 293 K was generated (Fig. S40 and ESI Movie†). The AIMD trajectory shows that the small pore channels are closed spontaneously, hence, cannot accommodate guest molecules (Scheme 1).

To identify preferred binding sites of the adsorbate molecule in the large pore channels, we adopted the following procedure. We first obtain a set of coarsely determined binding sites for each guest and their corresponding orientations in a $1 \times 1 \times 2$ supercell of Al-MOF. Several such Al-MOF simulation boxes loaded with a guest molecule each are further optimised individually. Density functional theory (DFT) is employed for geometry optimisations. The corresponding binding energies (BEs) were calculated for each optimised configuration. The range of binding energies (BEs) for guest molecules show good agreement with the experimentally measured isosteric heats of adsorption at near-zero coverage [$Q_{st}(0)$] (Fig. S26 and Table S4†)—CO_2 (BE = −19.1 to −36.0 kJ mol^{-1}; $Q_{st}(0)$ = −24.6 kJ mol^{-1}), C_2H_2 (BE = −34.5 to −37.3 kJ mol^{-1}; $Q_{st}(0)$ = −40.2 kJ mol^{-1}), C_2H_4 (BE = −33.2 to −38.7 kJ mol^{-1}; $Q_{st}(0)$ = −32.8 kJ mol^{-1}), C_2H_6 (BE = −34.8 to −39.9 kJ mol^{-1}; $Q_{st}(0)$ = −45.0 kJ mol^{-1}), CH_4 (BE = −25.2 to −25.4 kJ mol^{-1}; $Q_{st}(0)$ = −22.0 kJ mol^{-1}). In Fig. 1e, f and 2e, f, specific interactions such as hydrogen bonding, π-interactions, and Lewis acid–base pairs are depicted with relevant distances and/or angles. While these interactions aid in the adsorption of a guest molecule onto the surface of the pore channel, the affinity is predominantly due to dispersion interactions. To demonstrate the same, heavy (non-hydrogen) atoms that lie within 4 Å to any heavy atom of the guest molecule are represented as spheres in prominent figures (Fig. 1e, f and 2e, f).

The primary binding sites of CO_2, CH_4, and C_2H_6 are the corners of a pore channel. Corners allow a CO_2 molecule to participate in two weak hydrogen bonds and interact with two other carboxylate oxygen atoms of the framework (Fig. 2f) while enabling a C_2H_6 molecule to interact *via* hydrogen bonding with two framework carboxylate oxygen atoms (Fig. 1e). In contrast, C_2H_2 and C_2H_4 primarily bind to an edge. The π-clouds on these guests favour π-interactions with those of the naphthalene rings of the framework; however, additionally, they allow the guests to participate in one weak hydrogen bond each (Fig. 1f and 2e). Furthermore, binding sites close to an edge of a pore channel for CO_2/C_2H_6 and near the corner for C_2H_2/C_2H_4 exist, as shown in Fig. S21–S24.†

The isosteric heats of adsorption (Q_{st}) for CO_2 and C_2H_2 are nearly coverage-independent. In contrast, Q_{st} values for both C_2H_4 and C_2H_6 show a nearly monotonic increase with loading (Fig. 1b and S12†). Despite having a much smaller Q_{st} at near-zero coverage, the former increases rapidly with loading, thus surpassing the latter at a coverage of 0.92 mmol g^{-1} or about two molecules per unit cell of Al-MOF. To delineate this phenomenon, we followed the same protocol as that of single-molecule binding energy calculations, but now with simulation boxes consisting of more guest molecules.

Since we have considered two-unit cells of Al-MOF for our calculations, we generated initial configurations with four and six (2 and 3 molecules per unit cell, respectively) C_2H_4 and C_2H_6

guest molecules. Now, as the simulation cell includes two large pore channels, the configurations were further classified as 2/0, 1.5/0.5, and 1/1 configurations for two guest molecules per unit cell and likewise, 3/0, 2.5/0.5, 2/1, and 1.5/1.5 for three guest molecules per unit cell, depending on the number of guest molecules per pore channel per unit cell (Fig. S27–S39†). Following optimisation, in addition to binding energies (BE), we calculated the cooperative interaction energy (E_c) or the adsorbate–adsorbate interaction energies (see the ESI†). The average binding energies of molecules showed a steady increase with coverage for both C_2H_4 and C_2H_6 and to a greater extent when the molecules were concentrated in one of the channels. For 2/0 configurations, the binding energy for C_2H_6 and C_2H_4 was −43.1 and −41.1 kJ mol^{-1} (Table S5†), respectively, which are higher than their one molecule equivalents (Fig. S27, S30 and Table S4†). Three molecules per pore channel per unit cell (3/0) configuration were not obtained for C_2H_6, due to their large size.

In contrast, the binding energies ranged between −40.2 and −41.1 kJ mol^{-1} (Fig. S33†) for C_2H_4-3/0 configurations. Adsorbate–adsorbate interactions contribute significantly to the binding affinity, ranging between −5.6 and −6.9 kJ mol^{-1} (Table S5†). We speculate that the effect of cooperativity and hence the Q_{st} increase with higher coverage might be much more prominent in actual samples than in a small simulation box we considered in our calculations. However, the cross-over in Q_{st} *vs.* coverage between C_2H_4 and C_2H_6 does not affect the order of selectivity in equimolar mixture adsorption under ambient conditions. IAST calculations revealed that even at the highest pressure ($P/P_0 \sim 1$), the uptake amount of C_2H_4 is ∼0.5 mmol g^{-1}, much less than ∼0.92 mmol g^{-1} where the cross-over occurs (Fig. 1b and S12†).

Stepwise multicomponent dynamic breakthrough separation

Along with high thermal (∼450 °C) and moisture stability (Fig. S15†), the estimated mixed gas adsorption isotherm with excellent selectivity prompted us to explore the performance of the material under real-time conditions. A series of practical breakthrough experiments were carried out on Al-MOFM$_{15}$ for bi-component and quaternary-component gas mixtures. As shown in Fig. 3a, the C_2H_6/C_2H_4 mixture (0.5 : 0.5, v/v) was streamed through a packed column of activated adsorbent at the rate of 2.2–2.9 mL min^{-1} at 298 K. C_2H_4 can be detected first from the outlet gas runoff during the initial purges, resulting in a desirable high purity for more than 40 minutes, while no C_2H_6 was found. At approximately 45 minutes, as the adsorbent became saturated in the dynamic flow, C_2H_6 reached its breakthrough point as detected in the outlet downstream. Perceptibly, the C_2H_6 selective Al-MOFM$_{15}$ allows early release of pure C_2H_4, significantly simplifying the purification of this major petrochemical feedstock. However, as soon as the outlet stream reaches equal proportion, by closing the feed flow and only allowing the carrier gas, the absorbed C_2H_6 could be

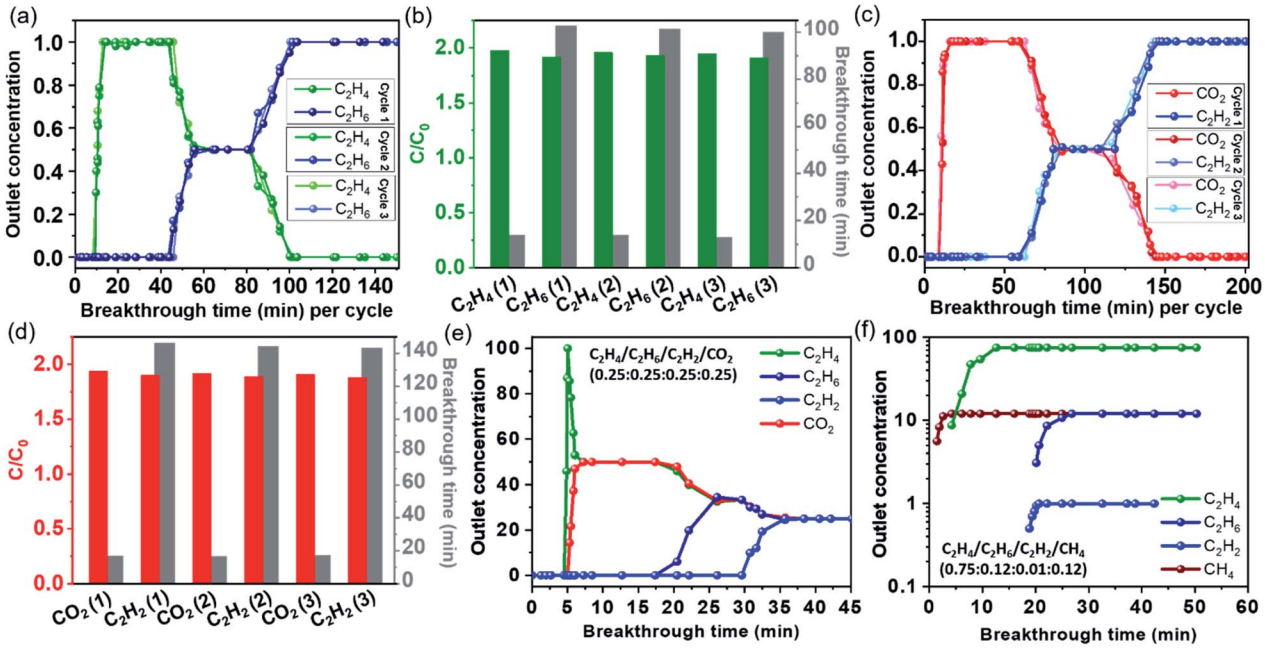

Fig. 3 (a) Experimental stepwise dynamic column breakthrough curves for 0.5 : 0.5 (v/v) C_2H_6/C_2H_4 gas mixture and (b) the corresponding maximum release concentration (outlet/feed; C/C_0) in the outlet of each component with time for three consecutive cycles. (c) Experimental stepwise dynamic column breakthrough curves for 0.5 : 0.5 (v/v) C_2H_2/CO_2 gas mixture and (d) the corresponding maximum release concentration (outlet/feed; C/C_0) in the outlet of each component with time for three consecutive cycles. Quaternary mixture separations of (e) $C_2H_4/C_2H_6/C_2H_2/CO_2$ (0.25 : 0.25 : 0.25 : 0.25) and (f) $C_2H_4/C_2H_6/C_2H_2/CH_4$ (0.75 : 0.12 : 0.01 : 0.12). The continuous flow was regulated by a mass flow controller using helium as the carrier gas with a total flow rate of 2.2–2.9 and 3.2–3.5 mL min^{-1} for binary and quaternary separations, respectively. The breakthrough experiments were studied in an adsorbed bed packed with ∼1.048 g of Al-MOFM$_{15}$ at 298 K and 1.05 bar. The packed column dimensions are 16.5 cm in length and 0.3 cm in diameter.

removed by regenerating the column for subsequent separations. To confirm the regeneration of Al-MOFM$_{15}$, we conducted a stepwise dynamic breakthrough for three consecutive cycles, and breakthrough times of the maximum release of each component are presented in Fig. 3b. Thereafter, a similar process was followed for the 0.5 : 0.5 mixture of C_2H_2/CO_2, CO_2/CH_4 and C_2H_6/CH_4. For C_2H_2/CO_2, CO_2 appears in the outlet flow as early as 10 minutes, while it took almost 6.5 times longer for C_2H_2 to reach its breakthrough point, revealing excellent separation performance for C_2H_2 from CO_2 (Fig. 3c and d). In contrast, for C_2H_6/CH_4 and CO_2/CH_4, C_2H_6 broke through the bed at 40 min, while it was 16 min for CO_2, as both C_2H_6 and CO_2 showed efficient adsorption over the weakly interacting CH_4 (Fig. S43 and S44†). It is worth noting that all breakthrough time intervals were tested multiple times through subsequent regeneration by flowing helium gas and were comparable, thus, showing the excellent reusability of the material (Fig. 3b and d).

The separation capacity of Al-MOFM$_{15}$ was further tested using a quaternary $C_2H_4/C_2H_6/C_2H_2/CO_2$ mixture. A sharp and pure separation of all four gases was observed with an early release of C_2H_4, with no evidence of CO_2, C_2H_2, or C_2H_6 in the first 5 minutes (Fig. 3e). Such a flawless separation of C_2H_4 with a high purity only through a single breakthrough separation is rarely found in the literature. Moreover, the traditional C_2H_4 production also co-exists with other by-products, mainly C_2H_6 with trace amounts of CH_4 and C_2H_2. So, this material was further investigated for the separation from a quaternary mixture of $C_2H_4/C_2H_6/C_2H_2/CH_4$ by mimicking its available industrial concentration (0.75 : 0.12 : 0.01 : 0.12, v/v). As shown in Fig. 3f, C_2H_4 appeared just after CH_4 within 5 minutes of gas flow, while highly efficient separation for even a trace amount (1%) of C_2H_2 was achieved by passing the mixture over a packed column of activated Al-MOFM$_{15}$. All the practical separation measurements are consistent with the experimental and simulated adsorption isotherm, selectivity and binding interactions.

Conclusions

In conclusion, we have developed a robust Al-based metal–organic framework by optimising the reaction time under microwave heating to achieve exclusive microporosity with high surface area. The foregoing results showed that the material ([Al(OH)(1,4-NDC)]·2H_2O) possesses not only extraordinary chemical and thermal stability but also exhibits exceptional sorption and selectivity performance of a tailor-made Al-MOF (Al-MOFM$_{15}$). It unveiled remarkable preferential interactions for C_2H_6 and C_2H_2 over C_2H_4 and C_2H_2 over CO_2, considered the most delicate combinations for separation in petroleum industries. The key to selectivity, as found, is a combination of multiple van der Waals interactions and suitable channel-like pores to match with different light hydrocarbons. At one end, single and mixed-gas adsorption, selectivity estimation, stepwise dynamic breakthrough separation from bi- and quaternary-component mixtures unfold extraordinary separation potency of such materials. On the other hand, the study also reveals the specific affinity of each hydrocarbon because of thermodynamic and kinetic predilections to the adsorbent as supported by binding energy estimation and molecular level visualisation through advanced molecular simulations.

Data availability

The data that support the findings of this study are available in the ESI of this article.†

Author contributions

TKM and SL designed the concept. SL and DR performed major experiments. ND and AS carried out the computational study under the guidance of SB. SL, ND, SB and TKM analysed the experimental and computational data and wrote the manuscript with inputs from all the co-authors.

Conflicts of interest

There are no conflicts to declare.

Acknowledgements

SL acknowledges DST-INSPIRE for the fellowship. ND thanks CSIR, India, for the fellowship. SB acknowledges the support and facility provided by 'PARAM Yukti Faculty' under the National Supercomputing Mission, Government of India, at the Jawaharlal Nehru Centre for Advanced Scientific Research, Bangalore, India. TKM is grateful to the Department of Science and Technology (DST, project no. CRG/2019/005951) for financial support.

Notes and references

1 D. S. Sholl and R. P. Lively, *Nature*, 2016, **532**, 435–437.
2 K.-J. Chen, D. G. Madden, S. Mukherjee, T. Pham, K. A. Forrest, A. Kumar, B. Space, J. Kong, Q.-Y. Zhang and M. J. Zaworotko, *Science*, 2019, **366**, 241.
3 N. A. Khan, Z. Hasan and S. H. Jhung, *Chem.–Eur. J.*, 2014, **20**, 376–380.
4 U. Wagner and H. M. Weitz, *Ind. Eng. Chem.*, 1970, **62**, 43–48.
5 R. Krishna, *ACS Omega*, 2020, **5**, 16987–17004.
6 L. Yang, S. Qian, X. Wang, X. Cui, B. Chen and H. Xing, *Chem. Soc. Rev.*, 2020, **49**, 5359–5406.
7 I. Amghizar, L. A. Vandewalle, K. M. Van Geem and G. B. Marin, *Engineering*, 2017, **3**, 171–178.
8 *Handbook of Industrial Hydrocarbon Processes*, ed. J. G. Speight, Gulf Professional Publishing, Boston, 2011, p. iii, DOI: DOI: 10.1016/B978-0-7506-8632-7.10020-9.
9 A. van Miltenburg, J. Gascon, W. Zhu, F. Kapteijn and J. A. Moulijn, *Adsorption*, 2008, **14**, 309–321.
10 L. Li, R.-B. Lin, R. Krishna, H. Li, S. Xiang, H. Wu, J. Li, W. Zhou and B. Chen, *Science*, 2018, **362**, 443.
11 Y. S. Ai-Zegbayer, S. I. Ai- Mayman and T. A. Ai-Smarei, *J. King Saud Univ., Eng. Sci.*, 2010, **22**, 21–27.
12 B. Zhu, J.-W. Cao, S. Mukherjee, T. Pham, T. Zhang, T. Wang, X. Jiang, K. A. Forrest, M. J. Zaworotko and K.-J. Chen, *J. Am. Chem. Soc.*, 2021, **143**, 1485–1492.

13 Z. Bao, D. Xie, G. Chang, H. Wu, L. Li, W. Zhou, H. Wang, Z. Zhang, H. Xing, Q. Yang, M. J. Zaworotko, Q. Ren and B. Chen, *J. Am. Chem. Soc.*, 2018, **140**, 4596–4603.
14 T. Ren, M. Patel and K. Blok, *Energy*, 2006, **31**, 425–451.
15 O. T. Qazvini, R. Babarao, Z.-L. Shi, Y.-B. Zhang and S. G. Telfer, *J. Am. Chem. Soc.*, 2019, **141**, 5014–5020.
16 H. Bux, C. Chmelik, R. Krishna and J. Caro, *J. Membr. Sci.*, 2011, **369**, 284–289.
17 J.-R. Li, R. J. Kuppler and H.-C. Zhou, *Chem. Soc. Rev.*, 2009, **38**, 1477–1504.
18 J.-R. Li, J. Sculley and H.-C. Zhou, *Chem. Rev.*, 2012, **112**, 869–932.
19 A. Granada, S. B. Karra and S. M. Senkan, *Ind. Eng. Chem. Res.*, 1987, **26**, 1901–1905.
20 D. A. Plattner, Y. Li and K. N. Houk, Modern Computational and Theoretical Aspects of Acetylene Chemistry, in *Modern Acetylene Chemistry*, ed. P. J. Stang and F. Diederich, 1995, DOI: **10.1002/9783527615278.ch01**.
21 A. Hazra, S. Jana, S. Bonakala, S. Balasubramanian and T. K. Maji, *Chem. Commun.*, 2017, **53**, 4907–4910.
22 S. Bhattacharyya, A. Chakraborty, A. Hazra and T. K. Maji, *ACS Omega*, 2018, **3**, 2018–2026.
23 R. Matsuda, R. Kitaura, S. Kitagawa, Y. Kubota, R. V. Belosludov, T. C. Kobayashi, H. Sakamoto, T. Chiba, M. Takata, Y. Kawazoe and Y. Mita, *Nature*, 2005, **436**, 238–241.
24 R. W. Baker, *Ind. Eng. Chem. Res.*, 2002, **41**, 1393–1411.
25 V. Guillerm, Ł. J. Weseliński, Y. Belmabkhout, A. J. Cairns, V. D'Elia, Ł. Wojtas, K. Adil and M. Eddaoudi, *Nat. Chem.*, 2014, **6**, 673–680.
26 B. R. Barnett, S. T. Parker, M. V. Paley, M. I. Gonzalez, N. Biggins, J. Oktawiec and J. R. Long, *J. Am. Chem. Soc.*, 2019, **141**, 18325–18333.
27 R.-B. Lin, L. Li, H.-L. Zhou, H. Wu, C. He, S. Li, R. Krishna, J. Li, W. Zhou and B. Chen, *Nat. Mater.*, 2018, **17**, 1128–1133.
28 S. Laha, R. Haldar, N. Dwarkanath, S. Bonakala, A. Sharma, A. Hazra, S. Balasubramanian and T. K. Maji, *Angew. Chem., Int. Ed.*, 2021, **60**, 19921–19927.
29 R. Haldar, N. Sikdar and T. K. Maji, *Mater. Today*, 2015, **18**, 97–116.
30 D. Bloch Eric, L. Queen Wendy, R. Krishna, M. Zadrozny Joseph, M. Brown Craig and R. Long Jeffrey, *Science*, 2012, **335**, 1606–1610.
31 S. Yang, A. J. Ramirez-Cuesta, R. Newby, V. Garcia-Sakai, P. Manuel, S. K. Callear, S. I. Campbell, C. C. Tang and M. Schröder, *Nat. Chem.*, 2015, **7**, 121–129.
32 J. W. Yoon, Y.-K. Seo, Y. K. Hwang, J.-S. Chang, H. Leclerc, S. Wuttke, P. Bazin, A. Vimont, M. Daturi, E. Bloch, P. L. Llewellyn, C. Serre, P. Horcajada, J.-M. Grenèche, A. E. Rodrigues and G. Férey, *Angew. Chem., Int. Ed.*, 2010, **49**, 5949–5952.
33 J. E. Bachman, M. T. Kapelewski, D. A. Reed, M. I. Gonzalez and J. R. Long, *J. Am. Chem. Soc.*, 2017, **139**, 15363–15370.
34 L. Li, R.-B. Lin, R. Krishna, H. Li, S. Xiang, H. Wu, J. Li, W. Zhou and B. Chen, *Science*, 2018, **362**, 443–446.
35 D.-L. Chen, N. Wang, C. Xu, G. Tu, W. Zhu and R. Krishna, *Microporous Mesoporous Mater.*, 2015, **208**, 55–65.
36 Y. Chen, Z. Qiao, H. Wu, D. Lv, R. Shi, Q. Xia, J. Zhou and Z. Li, *Chem. Eng. Sci.*, 2018, **175**, 110–117.
37 Y. Chen, H. Wu, D. Lv, R. Shi, Y. Chen, Q. Xia and Z. Li, *Ind. Eng. Chem. Res.*, 2018, **57**, 4063–4069.
38 W. Liang, F. Xu, X. Zhou, J. Xiao, Q. Xia, Y. Li and Z. Li, *Chem. Eng. Sci.*, 2016, **148**, 275–281.
39 P.-Q. Liao, W.-X. Zhang, J.-P. Zhang and X.-M. Chen, *Nat. Commun.*, 2015, **6**, 8697.
40 H.-G. Hao, Y.-F. Zhao, D.-M. Chen, J.-M. Yu, K. Tan, S. Ma, Y. Chabal, Z.-M. Zhang, J.-M. Dou, Z.-H. Xiao, G. Day, H.-C. Zhou and T.-B. Lu, *Angew. Chem., Int. Ed.*, 2018, **57**, 16067–16071.
41 K.-J. Chen, G. Madden David, S. Mukherjee, T. Pham, A. Forrest Katherine, A. Kumar, B. Space, J. Kong, Q.-Y. Zhang and J. Zaworotko Michael, *Science*, 2019, **366**, 241–246.
42 Z. Xu, X. Xiong, J. Xiong, R. Krishna, L. Li, Y. Fan, F. Luo and B. Chen, *Nat. Commun.*, 2020, **11**, 3163.
43 A. Comotti, S. Bracco, P. Sozzani, S. Horike, R. Matsuda, J. Chen, M. Takata, Y. Kubota and S. Kitagawa, *J. Am. Chem. Soc.*, 2008, **130**, 13664–13672.
44 S. Głowniak, B. Szczęśniak, J. Choma and M. Jaroniec, *Adv. Mater.*, 2021, **33**, 2103477.
45 S. Laha, D. Rambabu, S. Bhattacharyya and T. K. Maji, *Chem.–Eur. J.*, 2020, **26**, 14671–14678.
46 S. Laha, A. Chakraborty and T. K. Maji, *Inorg. Chem.*, 2020, **59**, 3775–3782.
47 C. Gücüyener, J. van den Bergh, J. Gascon and F. Kapteijn, *J. Am. Chem. Soc.*, 2010, **132**, 17704–17706.
48 X. Zhang, J.-X. Wang, L. Li, J. Pei, R. Krishna, H. Wu, W. Zhou, G. Qian, B. Chen and B. Li, *Angew. Chem., Int. Ed.*, 2021, **60**, 10304–10310.
49 M. Sarker, H. J. An, D. K. Yoo and S. H. Jhung, *Chem. Eng. J.*, 2018, **338**, 107–116.
50 E. V. Alexandrov, A. V. Goltsev, R. A. Eremin and V. A. Blatov, *J. Phys. Chem. C*, 2019, **123**, 24651–24658.
51 X. Liu, X. Wang and F. Kapteijn, *Chem. Rev.*, 2020, **120**, 8303–8377.
52 Y. Hu, Y. Chen, Y. Liu, W. Li, M. Zhu, P. Hu, H. Jin and Y. Li, *Microporous Mesoporous Mater.*, 2018, **270**, 67–74.
53 A. Nuhnen and C. Janiak, *Dalton Trans.*, 2020, **49**, 10295–10307.
54 B. Li, Y. Zhang, R. Krishna, K. Yao, Y. Han, Z. Wu, D. Ma, Z. Shi, T. Pham, B. Space, J. Liu, P. K. Thallapally, J. Liu, M. Chrzanowski and S. Ma, *J. Am. Chem. Soc.*, 2014, **136**, 8654–8660.
55 J. Pires, M. L. Pinto and V. K. Saini, *ACS Appl. Mater. Interfaces*, 2014, **6**, 12093–12099.
56 A. L. Myers and J. M. Prausnitz, *AIChE J.*, 1965, **11**, 121–127.
57 D. Ma, Z. Li, J. Zhu, Y. Zhou, L. Chen, X. Mai, M. Liufu, Y. Wu and Y. Li, *J. Mater. Chem. A*, 2020, **8**, 11933–11937.
58 W. Gong, H. Cui, Y. Xie, Y. Li, X. Tang, Y. Liu, Y. Cui and B. Chen, *J. Am. Chem. Soc.*, 2021, **143**, 14869–14876.
59 T.-L. Hu, H. Wang, B. Li, R. Krishna, H. Wu, W. Zhou, Y. Zhao, Y. Han, X. Wang, W. Zhu, Z. Yao, S. Xiang and B. Chen, *Nat. Commun.*, 2015, **6**, 7328.

60 H. Yang, Y. Wang, R. Krishna, X. Jia, Y. Wang, A. N. Hong, C. Dang, H. E. Castillo, X. Bu and P. Feng, *J. Am. Chem. Soc.*, 2020, **142**, 2222–2227.

61 R.-B. Lin, H. Wu, L. Li, X.-L. Tang, Z. Li, J. Gao, H. Cui, W. Zhou and B. Chen, *J. Am. Chem. Soc.*, 2018, **140**, 12940–12946.